

the thermal infrared (TIR). The MIR is used for identifying “hot-spots”, localized regions of anomalously hot pixels in satellite measurements (Wright et al., 2004). The MIR can also be used from the ground or on airborne platforms to image the heat from forest fires (Lentile et al., 2006) or hot gases rising from volcanic vents (Francis et al., 1995) and to map temperatures in plumes (Sawyer and Burton, 2006) and on lava fields (Realmuto et al., 1992). The TIR has been used less frequently to study volcanic processes. This is largely due to the fact that sensitivity in this region peaks at terrestrial temperatures of 300 K, much lower than the temperature of a typical “hot-spot” or volcanic heat source, and because until recently thermal imagers operating in the TIR required expensive active detector cooling systems (nitrogen dewars or Stirling cycle coolers) to achieve good signal-to-noise performance (Derniak and Boremann, 1996). TIR instruments on satellites do use active cooling systems and in these cases the image data are used to monitor volcanic eruption clouds and discriminate them from meteorological clouds for aviation hazard warnings and for gas measurements (Prata, 2009). Pugnaghi et al. (2002) used the MIVIS (multi-spectral infrared and visible imaging spectrometer) on board an aircraft to map the SO₂ emissions from Etna. Their algorithm was based on a split-window formulation using channels centred at 8.74 μm and 9.56 μm to eliminate the effects of water vapour and determine SO₂ abundance. Realmuto et al. (1994, 1997) showed that SO₂ could be determined from the multi-channel TIR imager ASTER (Advanced Space-borne Thermal Emission And Reflection Radiometer), on board the EOS Terra satellite, by using detailed radiative transfer calculations to account for water vapour and surface emissivity variations.

All of the work described above has used passive thermal sensing, relying on emission or absorption by the gas to provide a signal to measure. Measurements can also be made in absorption mode by using the sun as a source or by providing an artificial source of radiation (typically a globar and retroreflector). In these applications single field-of-view (fov), medium-spectral resolution (6 – 0.5 cm⁻¹) interferometers are used to gather quantitative information on multiple gas species simultaneously. Fourier-Transform Interferometers (FT-IRs) have become a very valuable device for volcanic

1155

gas studies (Love et al., 1998; Oppenheimer et al., 1998; Burton et al., 2000; Horrocks et al., 2001), including measurements of gas ratios reported by Oppenheimer et al. (2002). Systems using ultra-violet light as a source have recently been developed for volcanic SO₂ measurements (McGonigle, 2005; Horton et al., 2006), for volcanic BrO measurements (Bobrowski et al., 2003), and also for CO₂ slant-path columns (Goff et al., 2001). More recently Stremme et al. (2013) and Krueger et al. (2013) presented measurements of volcanic emissions using a scanning FT-IR, showing two dimensional visualisations of SO₂ based on thermal emission spectroscopy. Kinoshita et al. (2003) used a ground-based CCD imager together with a near infrared filter to study volcanic plumes, but they did not attempt a quantitative retrieval of the gases or particulates. Notsu et al. (2003) demonstrated the feasibility of using the 8.6 μm waveband for the measurement of volcanic SO₂ slant column density using a portable spectral infrared radiometer.

This paper presents the first detailed study of the use of a ground-based, uncooled thermal imaging radiometer to detect and quantify SO₂ gas from volcanic and industrial sources. The intention of this work was to develop a multi-filter TIR imaging camera capable of sensing gases and particles, principally for applications in volcanology. The details concerning the methods for detecting volcanic ash particles have been provided in a separate paper (Prata and Bernardo, 2009); here we concentrate on the SO₂ gas retrieval methodology. The capability to acquire frequent, real-time images from a fixed platform (e.g. located at a volcanological observatory near to an active volcano, or during a field deployment) day or night offers a practical and safe tool for understanding one aspect of volcanic activity.

The organisation of the paper is as follows: we briefly describe the principal characteristics of uncooled microbolometer thermal imaging devices and then show how such cameras can be adapted for use in detecting and quantifying SO₂ gas emissions. The design of the camera system is described and the basic theory presented for SO₂ slant column density (hereafter referred to as SCD) retrieval and then illustrated by showing how SO₂ emissions from an industrial stack can be derived. This is followed

1156

by a detailed error analysis of the retrieval scheme. Measurements made at two volcanoes, Etna, Sicily, Italy and Stromboli, Aeolian islands, Italy, are provided to show how estimates of volcanic SO_2 flux rates can be found. We end with some discussion on how this technology might be improved by integrating it with other remote sensing instruments, for example UV (Ultra-Violet) spectrometers, and used for quantitative studies of volcanic emissions, for detecting hazards from an airborne platform, and for alerting authorities of volcanic activity during the day and night for hazard warnings.

2 Thermal imagers

In the last 10–15 yr great advances have been made in manufacturing bolometers of high sensitivity (Kruse, 2001). The detectivity of these devices is background limited and they are often referred to as BLIP (background limited infrared photodetectors) devices. The use of silicon semiconductors (silicon nitride substrate with vanadium oxide detecting material) for manufacturing arrays of bolometric detectors has greatly reduced the cost of the production of thermal imaging cameras. These microbolometers, typically consist of 10^4 – 10^6 elements, are sensitive to radiation in the wavelength range of 7–14 μm and operate at 30–60 Hz (Kruse, 2001). Thermal cameras are commercially available with temperature sensitivities of ~ 50 mK (7–14 μm), array sizes of 320×240 pixels (or larger), F1.0 optics and 60 Hz operation. Thus in principle a camera of this kind can acquire images showing temperature changes of less than 0.1 K at a rate of 10's of frames per second. In practice this is difficult to achieve because of the presence of noise ($1/f$, background and internal temperature fluctuations, and Johnson noise), non-uniformity of the array, the need for calibration and frame integration. Other factors may also limit achieving the ideal image capture rate: for example extracting the image frame data rapidly requires fast electronics and a good microprocessor and communications hardware and software.

Shaw et al. (2005) describe an uncooled thermal imaging camera for use in atmospheric studies. This camera has a single passband (~ 8 –14 μm) and is used to view

1157

the sky overhead for studies of clouds. They report the calibration error of this instrument to be $0.5 \text{ W m}^{-2} \text{ sr}^{-1}$ or about 2% of the ambient radiance and also show that the microbolometer is sensitive at low temperatures (< 240 K) by observing changes in signals for very high thin clouds (cirrus). The camera developed here incorporates wavelength selection (filters) and this decreases the sensitivity and adds time delays to the image capture. The camera needs to be sensitive at temperatures of 230–300 K, which cover the typical range of atmospheric plume temperatures. In this paper we describe, in general terms, the thermal imaging camera and its modifications for use as an apparatus for quantifying atmospheric SO_2 gas emissions, and provide an error analysis with some illustrative examples of data captured at an industrial stack and at two erupting volcanoes.

3 Cyclops – a multifilter thermal infrared camera system

A commercial off the shelf (COTS) thermal IR (Infra-Red) camera with 50 mK noise-equivalent temperature difference ($\text{NE}\Delta T$) with a single, broadband filter covering the IR wavelength region from 7 μm to about 14 μm , was adapted for use in this work. A schematic of the principal components of the camera, “Cyclops” is provided in Fig. 1.

Radiation enters through the foreoptics (1), which defines the field of view and is focussed onto the microbolometer array (2). Readout electronics (3) converts the sensed radiation signals into voltages and a digitiser (4), microprocessor (5) and communications port (6) deliver the IR microbolometer array output to a computer for image display and further analysis. For use in detecting and quantifying atmospheric gases at typical atmospheric temperatures, several modifications to the COTS camera are needed. Figure 2 shows photographs of the camera and its main components. Figure 2a illustrates the filter set-up; Fig. 2b shows the camera body – the larger diameter housing holds the filter wheel, filters and the blackbody shutter; Fig. 2c shows the camera mounted on the deck of a ship with a calibration rig attached and an external shutter used to verify the internal shutter calibration. It is important to note that the design concept requires

1158

The impact of assuming that the plume temperature is constant through the plume could be significant because the thermal contrast of the plume contributes significantly to the SO₂ signal through Eq. (22). In the early stages of generation, the plume is likely to be very inhomogeneous and in thermal disequilibrium. When the plume has been generated from a large explosive eruption, it may remain inhomogeneous for tens of minutes⁴. An idea of the plume temperature variation can be obtained from an analysis of the broadband (7–14 μm) channel data. These data are the least noisy and the variation can be used as a proxy for the variation in the thermodynamic temperature structure. The coefficient of variation for the stable plumes studied here is ~0.01, and the typical temperature variability along the axis of the plume is ±3 K. If it is assumed that these metrics also apply to the thermodynamic temperature and that the magnitude of the variability does not change with position within the plume, then use of Eq. (22) with the plume temperature perturbed by ±3 K, gives SCD retrieval errors of 12–14 %.

Information about the spatial variation of the SO₂ absorption coefficient is not available. There is a small pressure and temperature dependence of the absorption coefficient, but given that the range of variability of pressure and temperature is small for the observing conditions, this dependence may be neglected.

Assumption (5) has been examined by use of the water vapour transmission model of Davis and Viezee (1964). The model asserts that the water vapour transmission (τ_λ) within the window region 8–12 μm is governed by,

$$\tau_\lambda = \exp\{-k_\lambda(P^*w)^{a_\lambda}\}, \quad (38)$$

where λ is wavelength, w is the precipitable water amount (in cm), P^* is the effective pressure, $P^* = P/P_s$, P = pressure (mb), P_s is the surface pressure, k_λ are the absorption coefficients and a_λ are coefficients determined by comparing the model with experimental measurements. The coefficients k_λ and a_λ are tabulated at 25 cm⁻¹ intervals from 800–1200 cm⁻¹. The model was used to compute the transmission over the

⁴We only consider eruptions where VEI < 3.

8.6 μm and 12 μm filter response functions⁵ as a function of water vapour amount, up to 5.5 cm of precipitable water. A measure of the difference between absorption at 8.6 and 12 μm is computed as $\text{Err} = (\tau_{8.6} - \tau_{12})/\tau_{8.6} \times 100\%$. Largest error (Err) is found for greatest precipitable water amounts and reaches about 10 % at 5 cm. We put an upper bound on the error due to assumption [5] as 10 % and the impact of this error on the retrieved SCD is at most a 3 % positive bias; that is higher SCDs are recovered under this assumption.

The assumption that the atmosphere is the same whether or not the plume is present seems intuitively reasonable as the atmospheric path under consideration is much larger than the path within the plume. Also, the atmospheric radiance is calculated by a linear or quadratic interpolation of the atmospheric radiance above and below the plume. The very linear nature of the fit obtained demonstrates that this is a good approximation. Nevertheless, there is error involved. This is estimated from the 1- σ uncertainty estimate obtained from the least squares fit. The uncertainty is evaluated for the 8.6 and 12 μm channels and for the difference. The 1- σ uncertainty for the difference was ±0.3 K, which translates to a SCD error of ±3 %.

4.2.3 Type III errors

Several of the parameters used in the retrieval scheme need to be specified. These include k_{SO_2} , geometry (elevation of the camera and field-of-view size of the camera), channel filter response functions, and the use of radiosonde data in the RT model. The absorption coefficient was obtained by integration over the filter response function using NIST values of the absorption coefficient measured at 0.125 cm⁻¹ resolution. The likely error incurred is small compared to other errors. An error in the absorption coefficient translates directly into an error in the retrieved SCD. We take this error as 1 %.

⁵It was found necessary to extrapolate the coefficients by 25 cm⁻¹ at both ends of the range in order to ensure the transmission profile was completely covered by the filter functions.

consecutive image frames (different spectral channels) separated by ~ 0.5 s that captured the rapid evolution of the cloud, when compared to an SO_2 gas emission. The ash cloud is also clearly discerned against the background atmosphere and the SO_2 gas, through its positive temperature difference anomaly. As with meteorological clouds, an ash cloud anomaly is easily identified and removed from the analyses (see also Fig. 16a). Having established that SO_2 can be identified and discriminated from other features, we now turn to the quantification of SO_2 retrieval and begin with a simple case where SO_2 is the only emission.

5.1 Port Pirie, South Australia

In order to test the ability of the camera to measure SO_2 , it was taken to a smelter and pointed towards a tall stack known to be emitting an SO_2 plume. The Port Pirie, South Australia (33.18° S, 138.02° E) lead smelter is the single largest lead smelter in Australia with mean SO_2 emissions of 1 kg s^{-1} ($\sim 80\text{--}130 \text{ t d}^{-1}$, see <http://www.epa.sa.gov.au/>). The plume is invisible to the eye (low water content) and emanates from a ~ 200 m tall stack. The camera was placed ~ 570 m from the stack and viewed it from the ground, looking upwards at an elevation angle of 15° with a clear blue sky background. Measurements were made continuously, which provided SO_2 estimates at intervals of 4–6 min. The length of time between samples is determined principally by the speed of data transfer and to a lesser degree by the need for capturing images at several wavelengths (different filters) and for acquiring calibration data. A typical sequence consisted of 5 measurements of the blackbody shutter (one measurement for each filter), followed by 5 measurements of the scene (the SO_2 plume), followed by a further 5 measurements of the blackbody shutter. Radiosonde profiles from Adelaide international airport (about 30 km distant) were acquired for use in calculating the water vapour corrections, however the corrections were small and below the noise limit of the camera and were not applied in the retrieval. The SO_2 signal was very large and clear in the data, however it was necessary to use a degree-2 polynomial fit to the brightness temperature-height profiles (Fig. 12).

1181

The final fits and retrieval were robust. Figure 13a–c shows a sequence of SO_2 retrievals illustrating the behaviour of the gas plume. At the start of the sequence (Fig. 13a) the plume rose ~ 50 m above the stack and then became bent over in the light winds. Later, the plume fumigated (Fig. 13b) and eventually with a change in wind speed and direction the plume became stronger and was carried away from the viewing site (Fig. 13c). It should be noted that with one camera it is not possible to discern the direction of travel of these gas plumes in the plane aligned with the camera viewing direction. For quantitative studies of gas plumes it would be preferable to use three cameras spaced at 120° to each other. The mean SCD for the Port Pirie plume on this day was $\sim 3 \times 10^{19} \text{ molecules cm}^{-2}$, with instantaneous maximum SCD near the stack exit exceeding $10^{20} \text{ molecules cm}^{-2}$. It is possible to estimate the average SO_2 flux from these data using estimates of the wind speed at stack height and the effective plume dimensions. An estimate of the SO_2 flux rate can be found from,

$$F = \rho Au, \quad (39)$$

where F is the flux rate (in kg s^{-1}), ρ is the concentration (in kg m^{-3}), A is the cross-sectional area of the plume (m^2) and u is the wind speed (in ms^{-1}) at plume height. Wind speeds at 200 m were $\sim 3\text{--}5 \text{ ms}^{-1}$ and the plume width (measured at half maximum) was taken as ~ 20 m (see Fig. 13). These values give fluxes of $\sim 1.5\text{--}2.5 \text{ kg s}^{-1}$, slightly higher than the mean emissions reported. In principle it is also possible to estimate the plume speed by tracking features in the plume (e.g. Bluth et al., 2007), however in the current configuration of the camera the data capture and calibration cycles require ~ 5 min to complete and thus feature tracking is not possible.

The camera was also tested at a second industrial site (a power station) in Victoria, Australia where several stacks were simultaneously imaged and SO_2 SCDs recovered. The success of these field trials at sites where SO_2 could be independently identified and measured gave us confidence to test Cyclops at active volcanoes.

1182

5.2 Etna

In September 2003 the camera was taken to Mt. Etna on the island of Sicily, to conduct SO₂ measurements under field conditions. Measurements were made from several locations, in most cases more than 10 km from the active vent. The retrieval of SO₂ from Etna is illustrated in Fig. 14. At one site, the camera was mounted on a rooftop in the village of Nicolosi, approximately 17 km from Etna and viewed the plume almost due N (350° azimuth) at an elevation angle of about 20°. At this low angle and distance, the water vapour path was significant and we regard this viewing configuration as being at the limit of the camera's capability. The data were acquired at 4–6 min intervals throughout the evening and into the following morning with no operator intervention and utilising automatic shutter calibration. The raw images were converted to brightness temperatures using pre-computed laboratory calibrations and adjusted using the off-set shutter calibration procedure. During the sequence of measurements the plume was blown in a NW direction and was confined to the boundary layer, remaining below ~ 5 km a.s.l. most of the time. In the morning, with the break-up of the nocturnal inversion layer, the plume was observed to rise (Fig. 14b). Some variability in the SO₂ gas emission rate was observed over the period with quiescent periods (Fig. 14e), strong puffing activity (Fig. 14f) and plume bifurcation (Fig. 14c and d).

Fluxes can be determined, as before, from Eq. (39). Values for A and u are not known accurately, but assuming the plume to be symmetric then the data suggest an average plume depth of ~ 500 m. The mean plume speed was estimated by running a trajectory model – HYSPLIT (Draxler and Rolph, 2003), starting from the summit elevation at 23:00 LT on 22 September 2003 and run forwards for 8 h. The trajectory of the plume found this way was towards the NW with a mean wind speed (over 8 h) of ~ 2 ms⁻¹. Using these values we find $F = \sim 10\text{--}20 \text{ kg s}^{-1}$ and the variation with time over 7 h of continuous measurements is shown in Fig. 15.

1183

5.3 Stromboli, Italy

Measurements at Stromboli were made on two separate occasions in late September 2003. Stromboli is an active stratovolcano which has been erupting and degassing SO₂ for at least 2000 yr. The effusive activity is observed from four vents near the summit and usually consists of small explosions followed by a period of quiescence which lasts from 10 min to a few hours. Very little ash was observed during the activity in September 2003. The Cyclops camera was used from two locations: near sea-level from the rooftop of a hotel (site A) and ~ 2.3 km ENE from the active crater, and nearer the volcano at Semaforo Labronzo (site B), 120 m a.s.l., and ~ 1.7 km north of the crater. At both locations the camera elevation was high (> 25°).

Long sequences of images were captured at both sites. The SO₂ plume was often mixed with water vapour (judged by its white appearance) and tended to erupt in puffs and disperse in the light winds (< 5 ms⁻¹). The retrievals indicate that total SO₂ SCDs varied from $1.1 \pm 0.2 \times 10^{18}$ – $3.1 \pm 0.6 \times 10^{18}$ molecules cm⁻² at site B and $1.4 \pm 0.3 \times 10^{18}$ to $2.3 \pm 0.5 \times 10^{18}$ molecules cm⁻² at site A. Individual plumes had variations from ~ 2×10^{17} to ~ 3×10^{18} molecules cm⁻², but these values are difficult to interpret in terms of concentrations because the plume depth is variable and unknown. Some examples of the retrievals at both sites are shown in Fig. 16. Measurements from site A were made in the late afternoon, and the gas emissions appeared to be continuous. At site B, measurements were made in the evening after the Sun had set and the gas emissions occurred frequently as discrete puffs. Explosions were also heard and several were imaged by the camera. Since the presence of ash can confound the retrieval scheme, it is important that the algorithm be insensitive to ash or be able to flag regions of the sky contaminated by ash. Figure 17a shows an occasion when an explosion occurred during the imaging. In this case the algorithm has rejected pixels that are ash contaminated and this is indicated on the image by the grey-coloured region. Within this region no SO₂ can be retrieved and consequently the total SCD for the whole plume will be underestimated.

1184

6 Conclusions

An instrument for measuring atmospheric gases using passive thermal infrared imaging radiometry has been successfully tested and a scheme for retrieving the SCD utilising multispectral imagery has been derived. The camera system was tested at two industrial sites and at two volcanic sites where plumes of SO₂ were present. The instrument proved reliable and was able to detect SO₂ in the presence of water vapour. Cloud features and ash particles that interfere with the SO₂ measurements could be detected using the multispectral nature of the imagery and removed from the analyses. The retrieval scheme proposed relies on spectral temperature difference measurements and is sensitive to channel NEΔT's estimated to be 0.1–0.8 K after frame averaging. The error on the retrieval was estimated to be ±20 %, due mostly to the NEΔT error, but with a significant error due to inaccurate measurement of the plume temperature. The bias error is estimated to be variable within the range –5 % to +6 %, which is slightly poorer than the calibration errors reported by Shaw et al. (2005) for their broadband camera.

The infrared camera is capable of providing 320 × 240 pixel images at frame rates as high as 60 Hz. However, it was found that noise considerations and data capture rates reduced this sampling frequency to several minutes. The limitation in sampling frequency is dominated by the slow data transfer rates, which can be easily overcome⁶. Faster sampling would allow measurements of the dynamic evolution of plumes and feature tracking could then be used as a means to determine gas flux rates. A more fundamental limitation is the NEΔT of the spectrally filtered channels. There are cameras available commercially with NEΔT's of 50 mK and 60 Hz frame rates that can provide retrieval errors in SCD below 10 %. Many improvements to the system can be envisaged. By viewing a target using three cameras arranged with an angular spacing of 120°, a 3-dimensional image could be acquired and quantitative measures of plume dimensions and plume morphology derived. Addition of filters centred at different

⁶The data transfer rate limitation is simply a feature of this particular thermal camera.

wavelengths would also permit a range of other gases to be measured. The camera could also be used in atmospheric research for studies of the radiative effects of clouds on the Earth's radiation balance (Smith and Toumi, 2008) and to image toxic gases from industrial accidents or from deliberate gas releases, where personal safety is a major issue.

The system described here has been operated from the ground, but it is quite feasible to use the system from an airborne platform. In this case, operation from higher altitude would permit use of spectral filters at wavelengths where water vapour is a problem in ground-based use. A filter situated near the 7.3 μm band would have 3 to 5 times the sensitivity to SO₂ as the 8.6 μm filter used here. One application for this technology in airborne use would be to mount the instrument to view forwards from a high altitude passenger jet aircraft. In this case it would be necessary to remove the filter wheel and use multiple cameras in order to achieve faster sampling rates. The cameras would offer the potential as an on board early warning device for hazards ahead of the aircraft (Prata and Barton, 1993). Hazards include volcanic ash and potentially clear air turbulence, detected through imaging water vapour anomalies. Enhanced night-time viewing capability is another feature of this technology that might be useful for jet aircraft.

Integration of the camera with other instruments is feasible. For example, infrasound arrays, ground-based lidars, ultra-violet cameras and spectrometers and FT-IRs all offer complementary information which would enhance the ability of a system for detecting a suite of gases, and for measuring their concentrations and fluxes (e.g. Lopez et al., 2013). Stand-off, 24 h, autonomous operation of the Cyclops camera has been demonstrated at two active volcanoes and plans are in place to deploy the system for long periods to test the durability of the instrument and the reliability of the detector calibration methodology employed.

Acknowledgements. The authors thank the reviewers for their helpful comments, particularly one reviewer for a very thorough and thoughtful review.

References

- Berk, A., Bernstein, L., Anderson, G., Acharya, P., Robertson, D., Chetwynd, J., and Adler-Golden, S.: MODTRAN cloud and multiple scattering upgrades with application to AVIRIS, *Remote Sens. Environ.*, 65, 367–375, 1998. 1176
- 5 Berk, A., Anderson, G. P., Bernstein, L. S., Acharya, P. K., Dothe, H., Matthew, M. W., Adler-Golden, S. M., Chetwynd Jr., J. H., Richtsmeier, S. C., Pukall, B., Allred, C. L., Jeong, L. S., and Hoke, M. L.: MODTRAN4 radiative transfer modeling for atmospheric correction, in: SPIE's International Symposium on Optical Science, Engineering, and Instrumentation, International Society for Optics and Photonics, 348–353, 1999. 1166
- 10 Bluth, G., Shannon, J., Watson, I., Prata, A., and Realmuto, V.: Development of an ultra-violet digital camera for volcanic SO₂ imaging, *J. Volcanol. Geoth. Res.*, 161, 47–56, 2007. 1182
- Bobrowski, N., Honninger, G., Galle, B., and Platt, U.: Detection of bromine monoxide in a volcanic plume, *Nature*, 423, 273–276, 2003. 1156
- Burton, M., Oppenheimer, C., Horrocks, L., and Francis, P.: Remote sensing of CO₂ and H₂O emission rates from Masaya Volcano, Nicaragua, *Geology*, 28, 915–918, 2000. 1156
- 15 Chu, P., Guenther, F., Rhoderick, G., and Lafferty, W.: The NIST quantitative infrared database, *J. Res. Natl. Inst. Stan.*, 104, 59–82, 1999. 1162
- Davis, P. and Vezee, W.: A model for computing the infrared transmission through atmospheric water vapour and carbon dioxide, *J. Geophys. Res.*, 69, 3785–3794, 1964. 1177
- 20 Darniak, E. and Boremann, G.: *Infrared Detectors and Systems*, John Wiley and Sons, Inc., 605 Third Avenue, New York, NY, 561 pp., 1996. 1155, 1173
- Draxler, R. and Rolph, G.: HYSPLIT (HYbrid Single-Particle Lagrangian Integrated Trajectory), NOAA Air Resources Laboratory, Silver Spring, MD, USA, model access via NOAA ARL READY, available at: <http://www.arl.noaa.gov/ready/hysplit4.html> (last access: 15 December 2013), 2003. 1183
- 25 Esler, M. B., Griffith, D. W., Wilson, S. R., and Steele, L. P.: Precision trace gas analysis by FT-IR spectroscopy. 1. Simultaneous analysis of CO₂, CH₄, N₂O, and CO in air, *Anal. Chem.*, 72, 206–215, 2000. 1154
- Francis, P., Maciejewski, A., Oppenheimer, C., Chaffin, C., and Caltabiano, T.: SO₂:HCl ratios in the plumes from Mt. Etna and Vulcano determined by Fourier Transform Spectroscopy, *Geophys. Res. Lett.*, 22, 1717–1720, 1995. 1155
- 30

1187

- Goff, F., Love, S. P., Warren, R., Counce, D., Obenholzner, J., Siebe, C., and Schmidt, S. C.: Passive infrared remote sensing evidence for large, intermittent CO₂ emissions at Popocatepetl Volcano, Mexico, *Chem. Geol.*, 177, 133–156, 2001. 1156
- Horrocks, L. A., Oppenheimer, C., Burton, M. R., Duffell, H. J., Davies, N. M., Martin, N. A., 5 and Bell, W.: Open-path Fourier transform infrared spectroscopy of SO₂: An empirical error budget analysis, with implications for volcano monitoring, *J. Geophys. Res.-Atmos.*, 106, 27647–27659, 2001. 1156
- Horton, K., Williams-Jones, G., Garbeil, H., Elias, T., Sutton, A., Mougini-Mark, P., Porter, J., and Clegg, S.: Real-time measurement of volcanic SO₂ emissions: validation of a new UV correlation spectrometer (FLYSPEC), *B. Volcanol.*, 68, 313–322, doi:10.1007/s00445-005-0026-5, 2006. 1156
- 10 Kinoshita, K., Kanagaki, C., Minaka, A., Tsuchida, S., Matsui, T., Tupper, A., Yakiwara, H., and Iino, N.: Ground and satellite monitoring of volcanic aerosols in visible and infrared bands, *CERes Int. Symp. On Remote Sensing – Monitoring of Environmental Change in Asia*, chiba, Japan, Dec., 16–17, 2003. 1156
- 15 Krueger, A., Stremme, W., Harig, R., and Grutter, M.: Volcanic SO₂ and SiF₄ visualization using 2-D thermal emission spectroscopy – Part 2: Wind propagation and emission rates, *Atmos. Meas. Tech.*, 6, 47–61, doi:10.5194/amt-6-47-2013, 2013. 1156
- Kruse, P.: *Uncooled Thermal Imaging: Arrays, Systems, and Applications*, SPIE Press (TT51), Bellingham, Washington, 90 pp., 2001. 1157
- 20 Lentile, L. B., Holden, Z. A., Smith, A. M., Falkowski, M. J., Hudak, A. T., Morgan, P., Lewis, S. A., Gessler, P. E., and Benson, N. C.: Remote sensing techniques to assess active fire characteristics and post-fire effects, *Int. J. Wildland Fire*, 15, 319–345, 2006. 1155
- Lopez, T., Fee, D., Prata, A., and Dehn, J.: Characterization and interpretation of volcanic activity at Karymsky volcano, Kamchatka, Russia, using observations of infrasound, volcanic emissions, and thermal imagery, *Geochem. Geophys. Geos.*, online first, doi:10.1002/2013GC004817, 2013. 1186
- 25 Love, S., Goff, F., Counce, D., Siebe, C., and Delgado, H.: Passive infrared spectroscopy of the eruption plume at Popocatepetl volcano, Mexico, *Nature*, 396, 563–567, 1998. 1156
- 30 McGonigle, A.: Volcano remote sensing with ground-based spectroscopy, *Philos. T. R. Soc. A*, 363, 2915–2929, 2005. 1156
- McMillin, L. and Crosby, D.: Theory and validation of the multiple window sea surface temperature technique, *J. Geophys. Res.*, 89, 3655–3661, 1984. 1168, 1176

1188

- Notsu, K., Mori, T., Igarashi, G., Tohjima, Y., and Wakita, H.: Infrared spectral radiometer: a new tool for remote measurement of SO₂ of volcanic gas, *Geochem. J.*, 27, 361–366, 2003. 1156
- Oppenheimer, C., Francis, P., Burton, M., Maciejewski, A., and Boardman, L.: Remote measurement of volcanic gases by fourier transform infrared spectroscopy, *Appl. Phys. B*, 67, 505–515, 1998. 1156
- 5 Oppenheimer, C., Edmonds, M., Francis, P., and Burton, M.: Variation in HCl/SO₂ gas ratios observed by fourier transform spectroscopy at Soufriere Hills, *Geol. Soc. London Mem.*, 21, 621–639, 2002. 1156
- Prata, A.: Satellite detection of hazardous volcanic clouds and the risk to global air traffic, *Nat. Hazards*, 51, 303–324, doi:10.1007/s11069-008-9273-z, 2009. 1155
- 10 Prata, A. and Barton, I.: Detection System for Use in an Aircraft, Australian Patent No PJ9518, European Patent No 91907594.5, US Patent, No. 5, 602 543, 1993. 1186
- Prata, A. and Bernardo, C.: Retrieval of volcanic ash particle size, mass and optical depth from a ground-based thermal infrared camera, *J. Volcanol. Geoth. Res.*, 182, 91–107, 2009. 1156, 1201
- 15 Prata, A., Bernardo, C., Simmons, M., and Young, W.: Ground-based detection of volcanic ash and sulphur dioxide, *Proc. of the 2nd International Conference on Volcanic Ash and Aviation Safety, OFCM (Washington DC), Alexandria, Virginia, USA*, 21–24, 2004. 1162
- Pugnaghi, S., Teggi, S., Corradini, S., Buongiorno, M., Merucci, L., and Bogliolo, M.: Estimation of SO₂ abundance in the eruption plume of Mt Etna using two MIVIS thermal infrared channels: a case study from the Sicily-1997 Campaign, *B. Volcanol.*, 64, 328–337, doi:10.1007/s00445-002-0211-8, 2002. 1155
- 20 Realmuto, V. J., Hon, K., Kahle, A. B., Abbott, E. A., and Pieri, D. C.: Multispectral thermal infrared mapping of the 1 October 1988 Kupaianaha flow field, Kilauea volcano, Hawaii, *B. Volcanol.*, 55, 33–44, 1992. 1155
- 25 Rothman, L. S., Barbe, A., Benner, D. C., Brown, L. R., Camy-Peyret, C., Carleer, M. R., Chance, K., Clerbaux, C., Dana, V., Devi, V. M., Fayt, A., Flaud, J.-M., Gamache, R. R., Goldman, A., Jacquemart, D., Jucks, K. W., Lafferty, W. J., Mandin, J.-Y., Massie, S. T., Nemtchinov, V., Newnham, D. A., Perrin, A., Rinsland, C. P., Schroeder, J., Smith, K. M., Smith, M. A. H., Tang, K., Toth, R. H., Vander Auwera, J., Varanasi, P., and Yoshino, K.: The HITRAN molecular spectroscopic database: edition of 2000 including updates of 2001, *J. Quant. Spectrosc. Ra.*, 82, 1–4, 2003. 1159
- 30

- Sawyer, G. M. and Burton, M. R.: Effects of a volcanic plume on thermal imaging data, *Geophys. Res. Lett.*, 33, L14311, doi:10.1029/2005GL025320, 2006. 1155
- Shaw, J., Nugent, P., Thurairajah, B., and Mizutani, K.: Radiometric cloud imaging with an uncooled microbolometer thermal infrared camera, *Opt. Express*, 13, 5807–5817, 2005. 1157, 1185
- 5 Smith, S. and Toumi, R.: Direct observation of cloudforcing by ground-based thermal imaging, *Geophys. Res. Lett.*, 35, L07814, doi:10.1029/2008GL033201, 2008. 1186
- Stemme, W., Krueger, A., Harig, R., and Grutter, M.: Volcanic SO₂ and SiF₄ visualization using 2-D thermal emission spectroscopy – Part 1: Slant-columns and their ratios, *Atmos. Meas. Tech.*, 5, 275–288, doi:10.5194/amt-5-275-2012, 2012. 1156
- 10 Strow, L. L., Hannon, S. E., Souza-Machado, D., Motteler, H. E., and Tobin, D.: An overview of the AIRS radiative transfer model, *IEEE T. Geosci. Remote*, 41, 303–313, 2003. 1176
- Wright, R., Flynn, L. P., Garbeil, H., Harris, A. J., and Pilger, E.: MODVOLC: near-real-time thermal monitoring of global volcanism, *J. Volcanol. Geoth. Res.*, 135, 29–49, 2004. 1155

Table 3. Polynomial fit coefficients for computing $NE\Delta T$ as a function of scene temperature and channel.

Channel (μm)	a_0	a_1	a_2	a_3
8.6	51.5922	-0.4982	1.634×10^{-3}	-1.803×10^{-6}
10	19.9328	-0.1856	5.906×10^{-4}	-6.333×10^{-7}
11	10.9692	-0.1009	3.186×10^{-4}	-3.380×10^{-7}
12	11.9301	-0.1102	3.531×10^{-4}	-3.833×10^{-7}
7–14	4.3983	-0.0421	1.352×10^{-4}	-1.450×10^{-7}

Table 4. Summary of error types and estimated error magnitudes.

Error type	Error source	Error in m_2 (in %; see Eq. 21).
I	$NE\Delta T$	$\pm 9\text{--}10$
I	Absolute calibration	± 5
II	RT model	± 2
II	Linearization	± 5
II	Plume temperature	$\pm 12\text{--}14$
II	Absorption coefficient spatial variability	(< 1 ?)
II	Transmission approximation	+3
II	Atmospheric invariance	± 3
III	Absorption coefficient	< 1
III	Geometry	< 0.5
III	Radiosonde	-

Table A1. List of symbols used.

$B[\lambda, T]$	=	Planck function
C_l	=	Camera line number
C_c	=	Camera column number
d	=	Plume thickness
F	=	Focal length of camera
I_i^b	=	Background radiance in channel i
I_i^f	=	Foreground radiance in channel i
I_i^p	=	Plume radiance in channel i
$k_{i,q}$	=	Absorption coefficient for channel i and absorber q
L	=	Path distance from camera to leading side of plume
m_q	=	Slant column density (SCD) ($= \rho_q d$) for absorber q
n	=	Pixel number
N_l	=	Number of lines in the image
N_c	=	Number of columns in the image
r	=	Radiation path in the direction θ, ϕ
r_1	=	Pathlength of plume radiation in the direction θ_n, ϕ_n
s_n	=	Size of pixel n
T_i^f	=	Foreground brightness temperature for channel i
T_i^o	=	Atmospheric brightness temperature "outside" the plume for channel i
T_i^p	=	Plume brightness temperature for channel i
T_p	=	Plume temperature
x, y, z	=	Cartesian coordinates as defined in Fig. 6
δT	=	Brightness temperature difference between the plume and the background for channel i
δT^*	=	Background brightness temperature difference between channel j and channel i
$\Delta T_{i,j}^p$	=	Plume brightness temperature difference between channel i and channel j
ΔT_i^p	=	Brightness temperature difference between plume temperature and background for channel i
ΔT_p^f	=	Temperature difference between the plume and channel i brightness temperature
λ	=	Wavelength (μm)
ϕ_n	=	Azimuthal angle of pixel n
Ψ	=	Angular field of view of camera
ρ_q	=	Density of absorber q
τ_i	=	Atmospheric transmission for channel i
θ_n	=	Elevation angle of pixel n
ζ	=	Elevation of camera measured to the first line of the image
χ	=	Detector chip pitch

1195

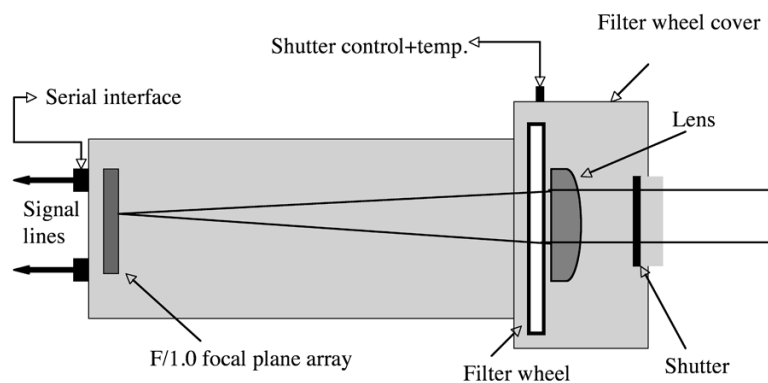


Fig. 1. Schematic showing the main components of the "Cyclops" thermal imaging infrared camera. Note that the filter wheel, containing up to 5 filters, is placed behind the lens.

1196

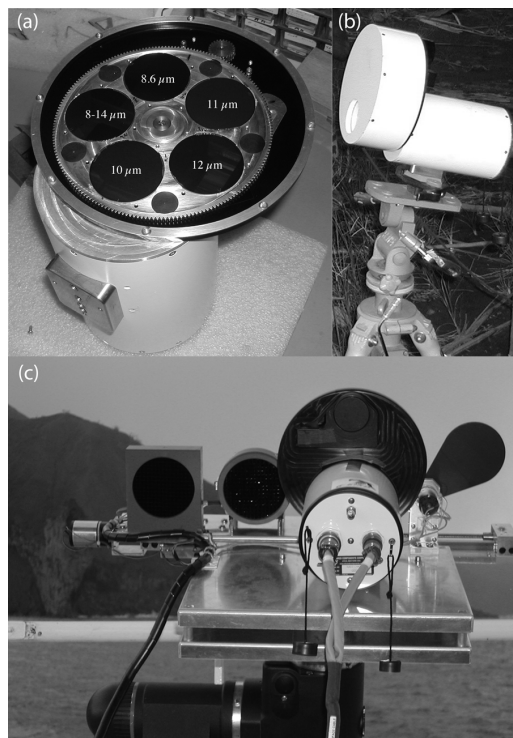


Fig. 2. (a) Filters mounted on filter wheel in the arrangement when used for measuring SO₂ gas emissions (central wavelengths in microns are given). (b) “Cyclops” camera mounted on a tripod for field operation. (c) Ship-mounted camera undergoing calibration tests with two moveable blackbodies and an external blackened shutter.

1197

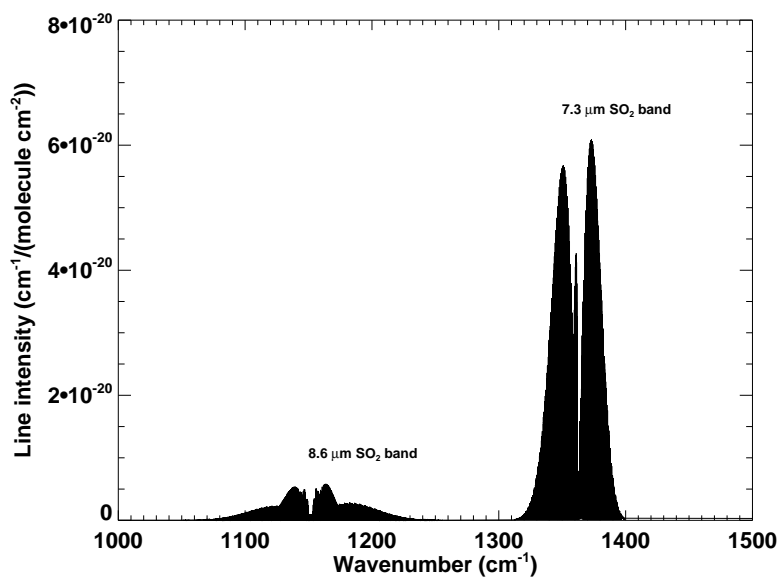


Fig. 3. SO₂ atmospheric transmission over the region 1000–1500 cm⁻¹ (6.7–10 μm).

1198

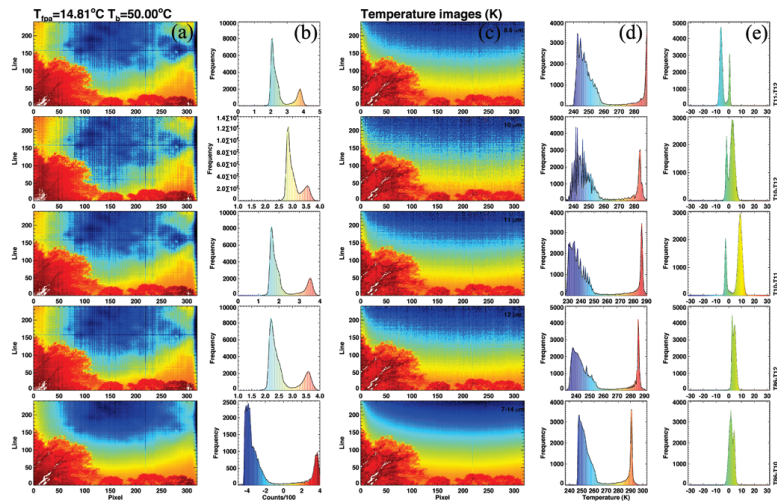


Fig. 4. Cyclops spectral images obtained at an SO₂-free, particulate-free site in Australia. **(a)** Panels showing uncalibrated data (DN's or Counts). **(b)** Their respective histograms. **(c)** Panels showing calibrated images. **(d)** Their histograms. **(e)** Histograms of selected temperature differences. The order of the images starting from the top is: 8.6, 10, 11, 12 μm and broadband (7–14 μm) channel.

1199

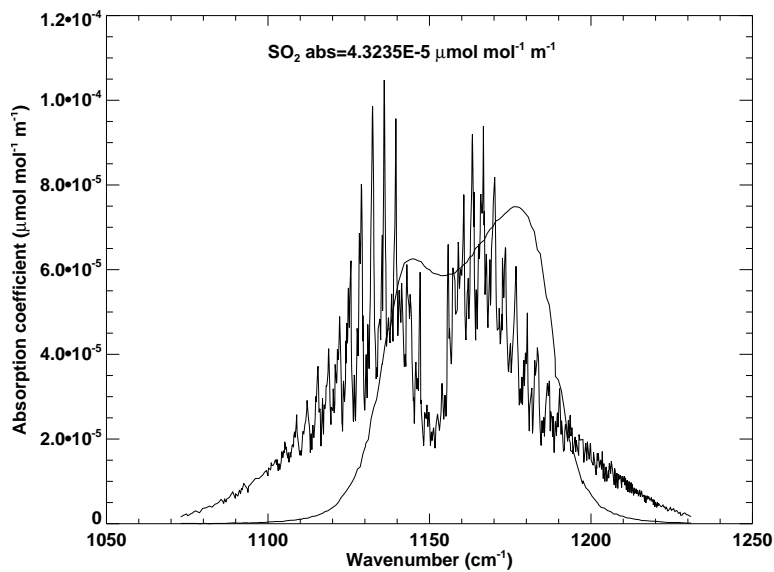


Fig. 5. Filter response function (smooth line) for the 8.6 μm Cyclops channel and the variation of the SO₂ absorption coefficient with wavenumber as measured by NIST. The integrated absorption coefficient over the waveband is $4.3235 \times 10^{-5} \mu\text{mol mol}^{-1} \text{m}^{-1}$.

1200

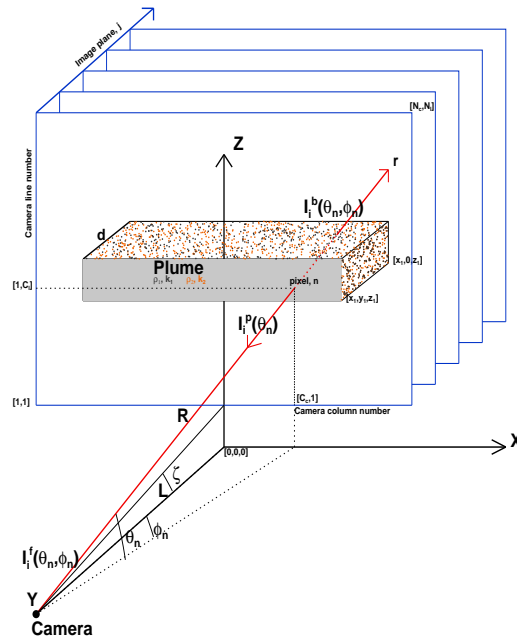


Fig. 6. Measurement geometry for a thermal camera viewing a distant SO₂ plume (after Prata and Bernardo, 2009).

1201

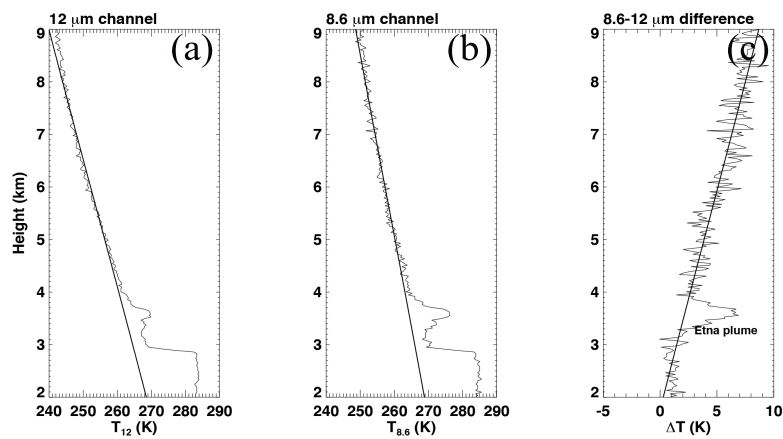


Fig. 7. (a) Brightness temperature vs. height variation for the 12 μm filter. (b) Brightness temperature vs. height variation for the 8.6 μm filter. (c) Brightness temperature difference vs. height variation for the 8.6–12 μm filters. The straight lines are least squares linear fits based on profile data above the plume, and extrapolated through and below the plume. ΔT is the brightness temperature difference between the 8.6 and 12 μm measurements.

1202

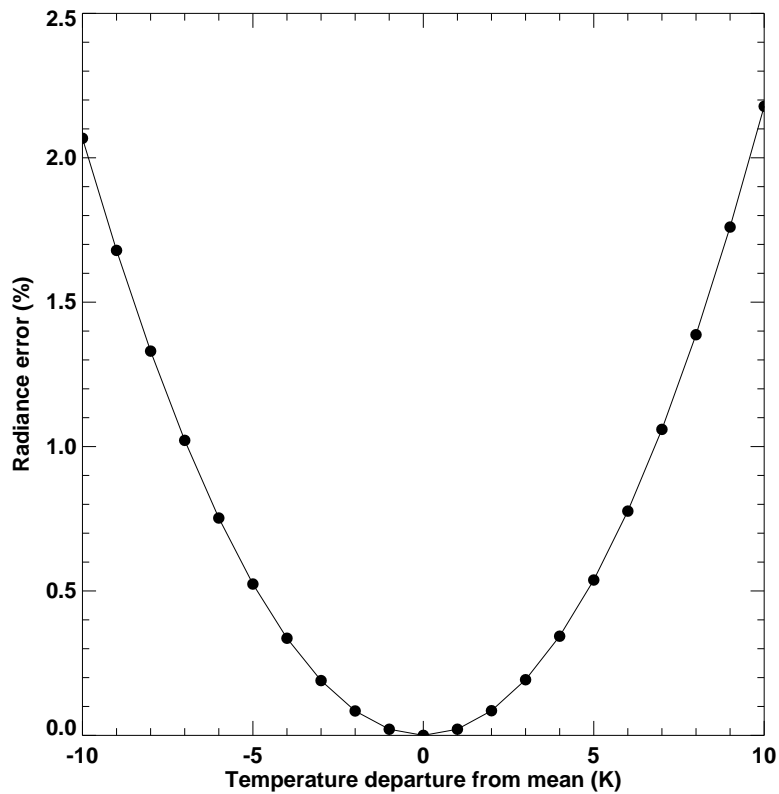


Fig. 8. Radiance error (in %) vs. departure from the mean temperature (K) caused by approximating the radiances using a 1st order Taylor series expansion about a mean temperature.

1203

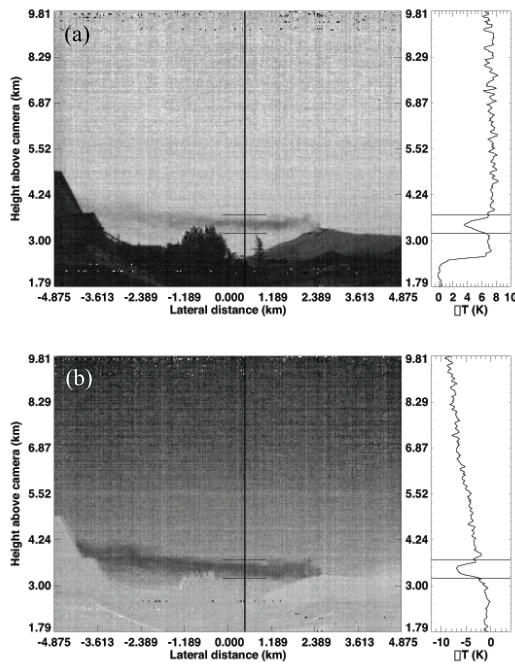


Fig. 9. (a) 12–11 μm brightness temperature difference image of the Mt Etna plume. The panel to the right shows a temperature difference-height profile for one image column, indicated by the vertical line on the image. (b) As for (a) but for the temperature difference between the 12 and 8.6 μm channels. The height profile for the same column as (a) is shown to the right of this image.

1204

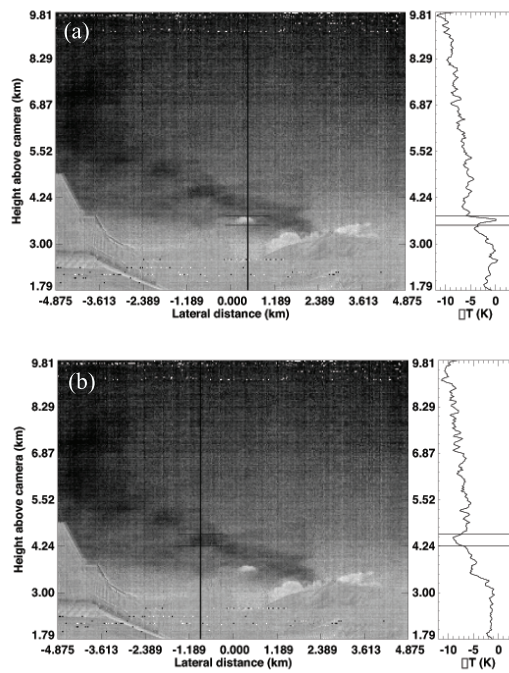


Fig. 10. (a) 12–8.6 μm brightness temperature difference image of the Mt Etna plume. The panel to the right shows a temperature difference-height profile for an image column that intersects a small meteorological cloud. (b) As for (a) but the height profile now intersects a portion of the Etna SO_2 plume.

1205

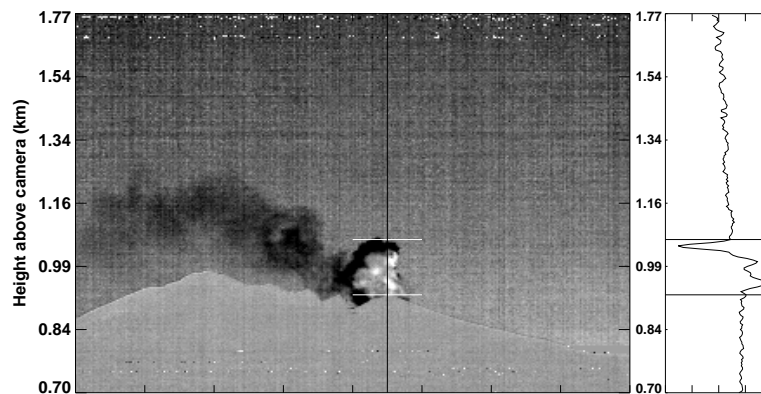


Fig. 11. 12–8.6 μm brightness temperature difference image of the Stromboli plume acquired during a small explosive eruption. The panel to the right shows a temperature difference-height profile for an image column that intersects the ash cloud eruption.

1206

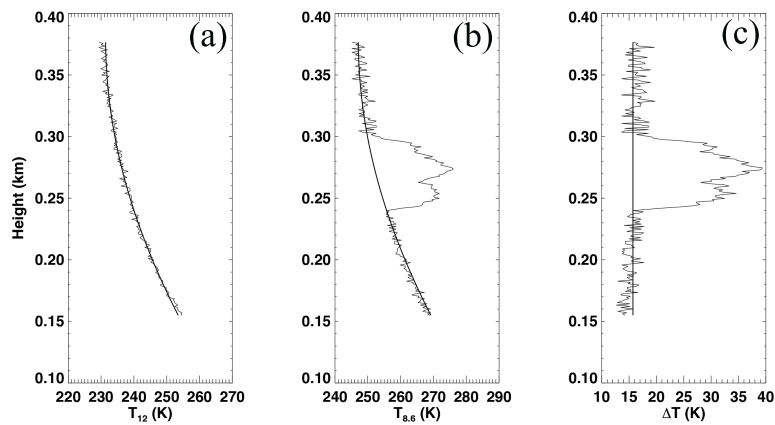


Fig. 12. (a) Brightness temperature vs. height variation for the 12 μm filter. (b) As for (a) but for the 8.6 μm filter. (c) The 8.6–12 μm brightness temperature difference. The curved lines are least squares degree-2 polynomial fits based on profile data above the plume, and extrapolated through and below the plume. ΔT is the brightness temperature difference between the 8.6 and 12 μm measurements.

1207

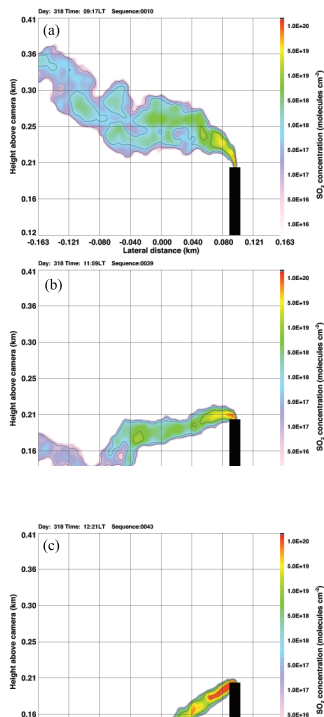


Fig. 13. Cyclops measurements of the SO_2 plume from the industrial stack at the Port Pirie lead smelter, showing different behaviours of the plume. (a) Lofted plume, (b) fumigation, and (c) grounding.

1208

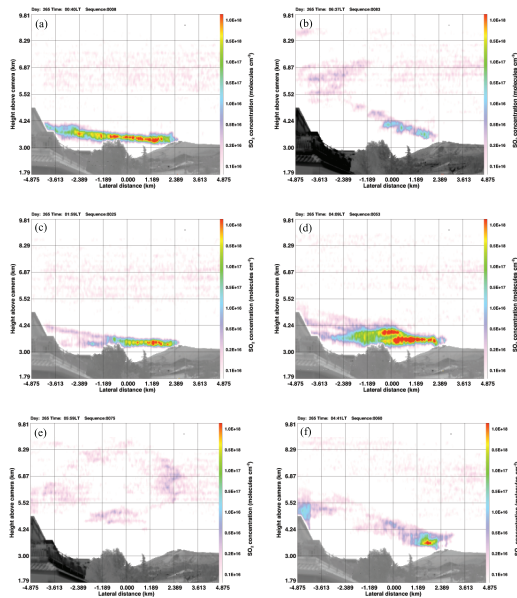


Fig. 14. Cyclops viewing a distant (~ 17 km) SO₂ plume from Mt Etna, Sicily. The frames illustrate different emission behaviour of the Etna plume. **(a)** Continuous gas emissions, trapped within the boundary layer. **(b)** Plume rise after the sun has risen. **(c and d)** Bifurcation of the plume – it is not possible to tell whether the bifurcating plumes are coplanar or whether one plume is moving away from or towards the camera. **(e)** Reduced activity with little or no gas plume visible. **(f)** Vigorous gas pulse with an indication of a column and some horizontal dispersion. Note that the apparent high SO₂ SCDs just below 5.52 km and near ~ -4.9 km are probably artefacts due to difficulties in calibrating the images on one part of the focal plane array.

1209

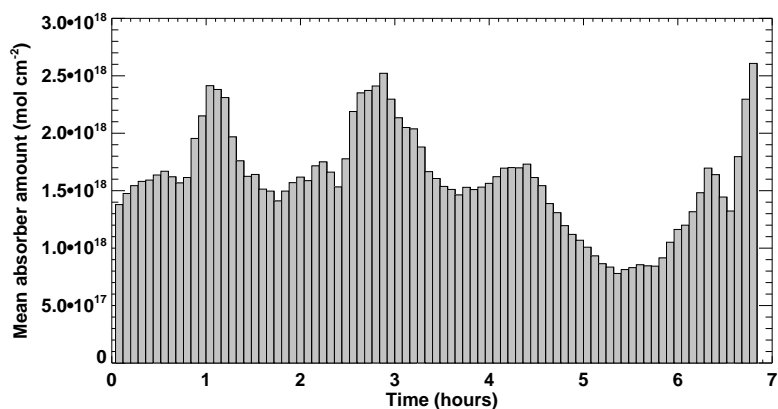


Fig. 15. Variation of the mean SCD (molecules cm⁻²) as a function of time for the Etna plume over a period of 7 h, starting from midnight until 07:00 LT the following day.

1210

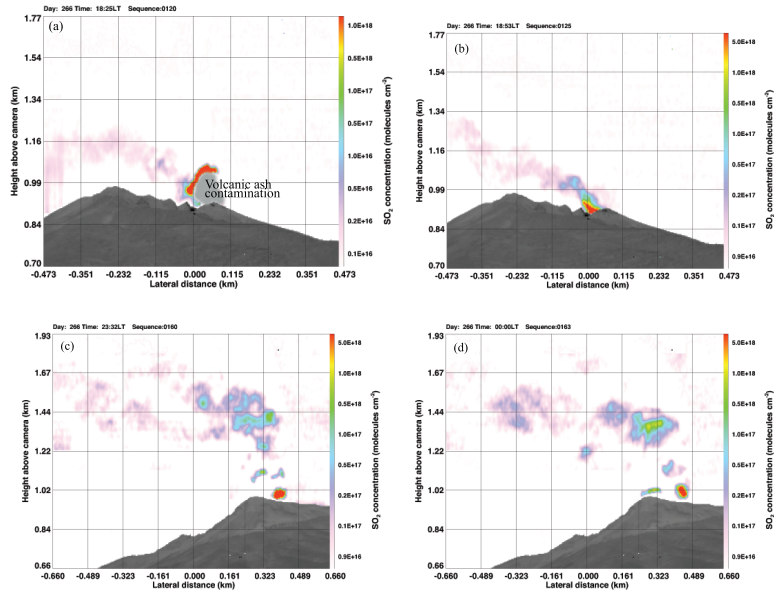


Fig. 16. Stromboli SO₂ observed from two different sites, ~ 1.7 km and ~ 2.3 km from the active crater. **(a)** shows an image where there was a small ash eruption obscuring the SO₂. The “ashy” parts of the cloud can be masked out by using different channels. Local Time (LT) = UTC + 2.